Formation of rarefaction waves in origami-based metamaterials

H. Yasuda,[1] C. Chong,[2,3] E. G. Charalampidis,[4] P. G. Kevrekidis,[4,5] and J. Yang[1,*]

[1]*Aeronautics & Astronautics, University of Washington, Seattle, WA 98195-2400, USA*

[2]*Department of Mechanical and Process Engineering (D-MAVT), Swiss Federal Institute of Technology (ETH), 8092 Zürich, Switzerland*

[3]*Department of Mathematics, Bowdoin College, Brunswick, Maine 04011, USA*

[4]*Department of Mathematics and Statistics, University of Massachusetts, Amherst, Massachusetts 01003-4515, USA*

[5]*Center for Nonlinear Studies and Theoretical Division, Los Alamos National Laboratory, Los Alamos, New Mexico 87544, USA*

(Received 12 May 2015; revised manuscript received 3 December 2015; published 15 April 2016)

We investigate the nonlinear wave dynamics of origami-based metamaterials composed of Tachi-Miura polyhedron (TMP) unit cells. These cells exhibit strain softening behavior under compression, which can be tuned by modifying their geometrical configurations or initial folded conditions. We assemble these TMP cells into a cluster of origami-based metamaterials, and we theoretically model and numerically analyze their wave transmission mechanism under external impact. Numerical simulations show that origami-based metamaterials can provide a prototypical platform for the formation of nonlinear coherent structures in the form of rarefaction waves, which feature a tensile wavefront upon the application of compression to the system. We also demonstrate the existence of numerically exact traveling rarefaction waves in an effective lumped-mass model. Origami-based metamaterials can be highly useful for mitigating shock waves, potentially enabling a wide variety of engineering applications.

DOI: 10.1103/PhysRevE.93.043004

I. INTRODUCTION

Recently, origami has attracted a significant amount of attention from researchers due to its unique mechanical properties. The most evident one is its compactness and deployability, which enables various types of expandable engineering structures, e.g., space solar sails [1,2] and solar arrays [3]. Biological systems also exploit such compact origami patterns, such as foldable tree leaves [4] and insect wings [5] for metabolic purposes. Another useful aspect of origami-based structures is that origami patterns can enhance static mechanical properties of structures. For instance, structural bending rigidity for thin-walled cylindrical structures can be significantly improved by imposing origami-patterns [6]. These origami patterns are used not only for space structures, but also in commercial products (e.g., beverage cans [7]) to reduce the thickness of thin-walled structures without sacrificing their buckling strength.

Within the considerable progress made in the mechanics of origami-based structures, however, the primary focus has been placed on the static or quasistatic properties of origami. For example, recent studies attempted to fabricate origami-based metamaterials with an eye toward investigating the deployable, auxetic, and bistable nature of origami structures [8–11]. Limited work has been reported on the impact response of origami-based structures [12], and their wave dynamics is relatively unexplored. Plausibly, this lack of studies on the dynamics of origami-based structures can be attributed to the intrinsic characteristic of typical origami structures, which exhibit limited degrees of freedom (DOF) during their folding and unfolding motions. This is particularly true for rigid origami, in which the deformation takes place only along crease lines, while origami facets remain rigid in dynamic conditions. The rigid origami features single-DOF motions ideally, and thus, the studies on their wave dynamics have been more or less absent under this rigid foldability assumption.

In this study, we use a single-DOF rigid origami structure as a building block to assemble multi-DOF mechanical metamaterials and analyze their nonlinear wave dynamics through analytical and numerical approaches. Specifically, we employ the Tachi-Miura polyhedron (TMP) [13,14] as a unit cell of the metamaterial as shown in Fig. 1. The TMP cell is made of two adjoined sheets [Fig. 1(a)], and changes its shape from a vertically standing planar body to a horizontally flattened one while taking up a finite volume between the two phases [Fig. 1(b)]. This volumetric behavior is in contrast to conventional origami-patterns that feature planar architectures and in-plane motions (e.g., Miura-ori sheets [15]). In this study, we first characterize the kinematics of the TMP cell, showing that it exhibits controllable strain-softening behavior. By cross-linking these TMP unit cells in a horizontal layer (e.g., see Ref. [11]) and stacking them up vertically with separators, we form a multi-DOF metamaterial as shown in Fig. 1(c). We then conduct analytical and numerical studies to verify that these multi-DOF origami structures can support a nonlinear stress wave in the form of a so-called rarefaction wave, owing to the strain softening nature of the assembled structure.

The rarefaction wave, which can be viewed as a variant of a depression wave [16], has been studied in various settings, including systems of conservation laws [17]. Recently, it was proposed in the context of discrete systems with strain-softening behavior [18,19]. Interestingly, these rarefaction waves feature tensile wavefronts despite the application of compressive stresses upon external impact [see the conceptual illustrations in Fig. 1(c)]. In that light, they are fundamentally different from the commonly encountered dynamical response of nonlinear elastic chains, which support weakly or even strongly nonlinear traveling compression waves [19–22]. More recently, strain-softening behavior was shown to be possible in tensegrity structures [23], where rarefaction waves were identified computationally in the elastic softening regime.

In the present work, we will study the formation and propagation of rarefaction waves in origami-based metamaterials via two simplified models: a multibar linkage model and a lumped-mass model. In both cases, we confirm that

*jkyang@aa.washington.edu

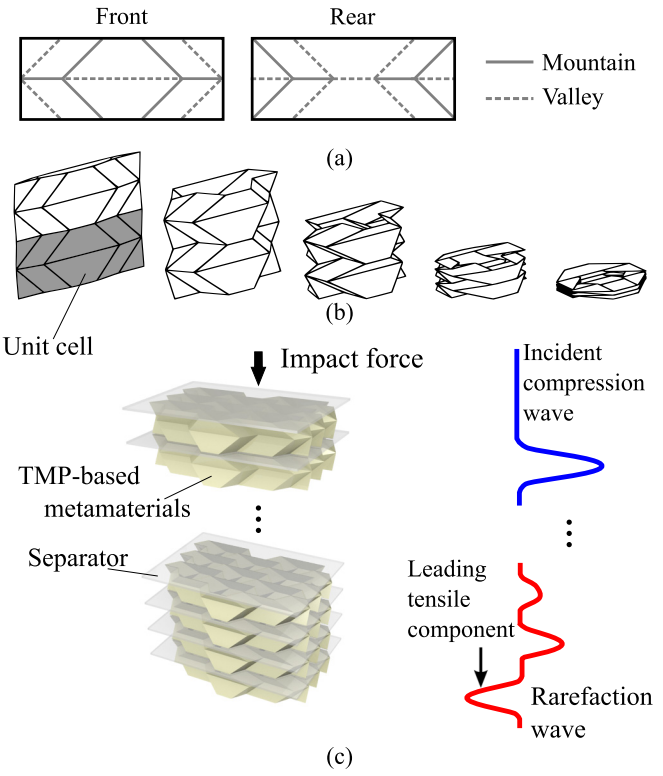

FIG. 1. (a) Flat front and rear sheets of the TMP with mountain (solid lines) and valley (dashed lines) crease lines. (b) Folding motion of the TMP unit cell. Shaded area is a unit cell of the TMP, which consists of the front and rear sheets shown in (a). (c) System consisting of TMP-based metamaterials and rigid separators stacked vertically. Each layer consists of nine interlinked TMP unit cells (see Ref. [11] for details of such horizontal clustering). Conceptual illustrations of incident compressive waves and transmitted rarefaction waves are also shown.

the origami structure disintegrates strong impact excitations by forming rarefaction waves, followed by other dispersive wave patterns to be discussed in more detail below. We also validate the nonlinear nature of the stress waves by calculating the variations of wave speed as a function of external force amplitude. Notably, we observe the reduction of wave speed as the excitation amplitude increases, which is in sharp contrast to conventional nonlinear waves seen in nature or engineered systems [19]. In the case of the lumped-mass model, we find numerically exact traveling waves. We provide a precise characterization of the wave speed and amplitude relationship and a way to evaluate the robustness of the rarefaction waves through dynamical stability computations. The findings in this study provide a foundation for building a new type of impact mitigating structure with tunable characteristics, which does not rely on material damping or plastic deformation. This study also offers a platform for exciting the rarefaction pulse—a far less explored type of traveling wave—and examining its characteristics in considerable detail.

The Manuscript is structured as follows: In Sec. II, we describe the two simple models of origami-based metamaterials: the multibar linkage model and the lumped-mass model. In Sec. III, we conduct numerical simulations of wave propagation upon impact on the chain boundary and compare the wave dynamics obtained from these two models. Then, in Sec. IV we find numerically exact rarefaction waves of the lumped-mass model and study the spectral and dynamical stability of rarefaction waves in Sec. V. Last, concluding remarks and future work are given in Sec. VI.

II. MODELING OF ORIGAMI-BASED STRUCTURES

A. Multibar Linkage Model

We begin by modeling a single TMP cell as shown in Fig. 2. For the sake of simplicity, we focus on the folding motion of two adjacent facets along the horizontal crease line as marked by the red line in Fig. 2(a). Preserving the key features of the TMP, such as rigid foldability and single-DOF mobility, we can model the folding and unfolding motion of the origami facets into a simple 1D linkage model as shown in Fig. 2(b). Here, the unit cell consists of two rigid bars (mass m and length $2L$), and the center-of-mass coordinates of those two bars are (z_1^L, y_1^L, θ_1) and $(z_1^R, y_1^R, \pi - \theta_1)$, where superscripts L and R denote left and right linkages, respectively. The hinge that connects the two bars is equipped with a linear torsional spring with the torsion coefficient k_θ. The left end of the linkage structure is supported by a roller joint, which is allowed to move only

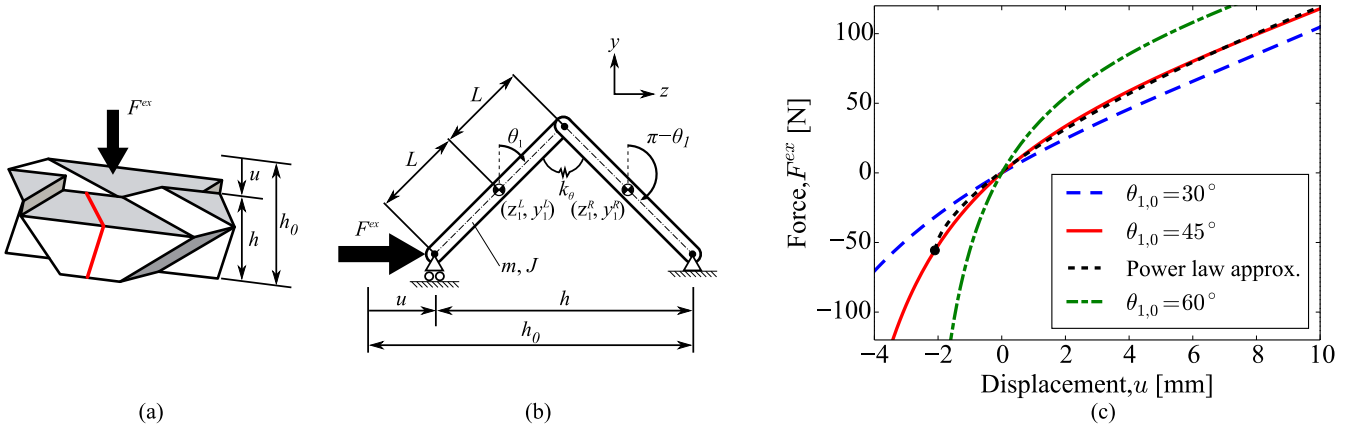

FIG. 2. (a) TMP unit cell. (b) Two-bar linkage model representing the folding motion of the two facets as marked in red lines in (a). (c) Force-displacement relationship of the TMP unit cell with $L = 5$ mm, $k_\theta = 1.0$ Nm/rad, and different initial folding angles: $\theta_{1,0} = 30^\circ$, 45°, and 60°. Dotted line indicates a power-law approximation of $\theta_{1,0} = 45^\circ$ case.

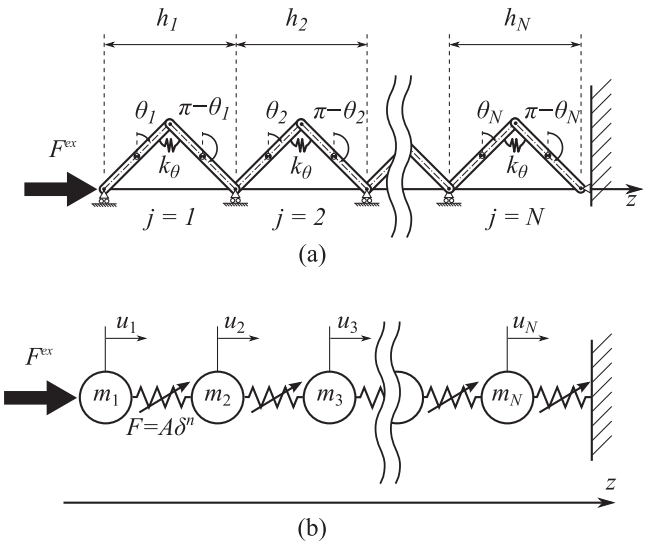

FIG. 3. Schematic illustrations of (a) multibar linkage model and (b) lumped-mass model.

along the z axis up on the application of external force F^{ex}. The right end is fixed by a pin joint. Therefore, the inclined angle of the linkage, θ_1, is the only parameter required to describe the motion of this unit-cell system. This corresponds to the single-DOF nature of the TMP cell.

Based on the single unit cell, we model a chain of N-TMP cells as shown in Fig. 3(a). In this model, each unit cell is connected by pin joints, which are allowed to move along the z axis. The center-of-mass coordinates of the two bars and the orientation angles for the jth unit cell are $(z_j^L,\ y_j^L,\ \theta_j)$ and $(z_j^R,\ y_j^R,\ \pi-\theta_j)$, respectively. Let us regroup this set of coordinates in a vector form as follows:

$$\boldsymbol{r}_j = \left[z_j^L,\ y_j^L,\ \theta_j,\ z_j^R,\ y_j^R,\ \pi-\theta_j\right]^T.$$

Then, the coordinate of the origami chain can be expressed as

$$\boldsymbol{r} = \left[\boldsymbol{r}_1^T, \ldots, \boldsymbol{r}_j^T, \ldots, \boldsymbol{r}_N^T\right]^T.$$

Introducing the general coordinate,

$$\boldsymbol{q} = [\theta_1,\ \ldots,\ \theta_j,\ \ldots,\ \theta_N]^T,$$

the velocity vector $\dot{\boldsymbol{r}}$ and the corresponding acceleration $\ddot{\boldsymbol{r}}$ can be expressed as

$$\dot{\boldsymbol{r}} = \boldsymbol{G}\boldsymbol{q}, \quad \ddot{\boldsymbol{r}} = \dot{\boldsymbol{G}}\dot{\boldsymbol{q}} + \boldsymbol{G}\ddot{\boldsymbol{q}}, \tag{1}$$

where

$$\boldsymbol{G} = \begin{bmatrix} \boldsymbol{G}_1 & \boldsymbol{g}_2 & \cdots & \boldsymbol{g}_j & \cdots & \boldsymbol{g}_N \\ \boldsymbol{O}_{6\times1} & \boldsymbol{G}_2 & \vdots & \boldsymbol{g}_j & \vdots & \boldsymbol{g}_N \\ \vdots & \boldsymbol{O}_{6\times1} & \ddots & \vdots & \vdots & \vdots \\ \vdots & \vdots & \ddots & \boldsymbol{G}_j & \vdots & \vdots \\ \vdots & \vdots & \vdots & \ddots & \ddots & \vdots \\ \boldsymbol{O}_{6\times1} & \boldsymbol{O}_{6\times1} & \cdots & \cdots & \cdots & \boldsymbol{G}_N \end{bmatrix},$$

$$\boldsymbol{G}_j = [-3L\cos\theta_j,\ -L\sin\theta_j,\ 1 \\ -L\cos\theta_j,\ -L\sin\theta_j,\ -1]^T,$$

$$\boldsymbol{g}_j = [-4L\cos\theta_j,\ 0,\ 0,\ -4L\cos\theta_j,\ 0,\ 0]^T,$$

$$\boldsymbol{O}_{6\times1} = [0,\ 0,\ 0,\ 0,\ 0,\ 0]^T.$$

If we fix the time and displacement under virtual velocity (i.e., $\delta\boldsymbol{q} = \boldsymbol{0}$ and $\delta t = 0$) [24], the variation of the velocity vector becomes

$$\delta\dot{\boldsymbol{r}}_j = \sum_{k=1}^{N} \frac{\partial\dot{\boldsymbol{r}}_j}{\partial\dot{q}_k}\delta\dot{q}_k. \tag{2}$$

Then the principle of virtual power is expressed by

$$\sum_{j=1}^{N} (\hat{\boldsymbol{M}}_j\ddot{\boldsymbol{r}}_j - \boldsymbol{f}_j)\cdot\delta\dot{\boldsymbol{r}}_j = 0, \tag{3}$$

where $\hat{\boldsymbol{M}}_j$ is a mass matrix expressed as

$$\hat{\boldsymbol{M}}_j = \text{diag}[m\ m\ J\ m\ m\ J],$$

and J is the bar's moment of inertia ($J = mL^2/3$). Also, $\boldsymbol{f}_j$ is a force vector defined as follows:

$$\boldsymbol{f}_j = \begin{cases} [F^{\text{ex}},\ 0,\ -2k_\theta(\theta_1-\theta_{1,0}) - F^{\text{ex}}L\cos\theta_1,\ 0,\ 0,\ -2k_\theta(\theta_{1,0}-\theta_1)]^T & \text{if } j=1 \\ [0,\ 0,\ -2k_\theta(\theta_j-\theta_{j,0}),\ 0,\ 0,\ -2k_\theta(\theta_{j,0}-\theta_j)]^T & \text{if } j=2\ldots N, \end{cases}$$

where $\theta_{j,0}$ is the initial folding angle of the jth unit cell (i.e., no torque applied at the hinge in this initial angle), and F^{ex} is the external force applied to the first unit cell as shown in Fig. 3(a). The advantage of the principle of virtual power is that we can apply it to a system with both motion and geometrical constraints, and we can derive the equation of motion without considering force constraints.

Substituting Eq. (2) into Eq. (3), we obtain

$$\sum_{k=1}^{N}\left[\sum_{j=1}^{N}(\hat{\boldsymbol{M}}_j\ddot{\boldsymbol{r}}_j - \boldsymbol{f}_j)\cdot\frac{\partial\dot{\boldsymbol{r}}_j}{\partial\dot{q}_k}\right]\delta\dot{q}_k = 0.$$

Therefore,

$$\sum_{j=1}^{N}(\hat{\boldsymbol{M}}_j\ddot{\boldsymbol{r}}_j - \boldsymbol{f}_j)\cdot\frac{\partial\dot{\boldsymbol{r}}_j}{\partial\dot{q}_k} = 0,$$

where $k = 1,\ \ldots, N$. Then

$$\boldsymbol{G}^T\hat{\boldsymbol{M}}\dot{\boldsymbol{v}} = \boldsymbol{G}^T\boldsymbol{f}, \tag{4}$$

where

$$\hat{\boldsymbol{M}} = \text{diag}\left[\hat{\boldsymbol{M}}_1\ \ldots\ \hat{\boldsymbol{M}}_N\right],$$

$$\boldsymbol{f} = \left[\boldsymbol{f}_1^T, \ldots,\ \boldsymbol{f}_j^T, \ldots,\ \boldsymbol{f}_N^T\right]^T.$$

Substituting Eq. (1) into Eq. (4), we obtain the equation of motion as follows:

$$\boldsymbol{G}^T\hat{\boldsymbol{M}}\boldsymbol{G}\ddot{\boldsymbol{q}} + \boldsymbol{G}^T\hat{\boldsymbol{M}}\dot{\boldsymbol{G}}\dot{\boldsymbol{q}} = \boldsymbol{G}^T\boldsymbol{f}. \tag{5}$$

To obtain the equation of motion of a unit cell, let us consider a simple case of $N = 1$. The position and velocity vectors of the two rigid bars in the unit cell [see Fig. 2(b)] are

$$\begin{aligned}
(z_1, y_1) &= (-3L\sin\theta_1,\ \ L\cos\theta_1),\\
(z_2, y_2) &= (-L\sin\theta_1,\ \ L\cos\theta_1),\\
(\dot{z}_1, \dot{y}_1) &= (-3L\dot{\theta}_1\cos\theta_1,\ \ -L\dot{\theta}_1\sin\theta_1),\\
(\dot{z}_2, \dot{y}_2) &= (-L\dot{\theta}_1\cos\theta_1,\ \ -L\dot{\theta}_1\sin\theta_1).
\end{aligned}$$

Note that the origin of z axis is located at the fixed wall. Then, we obtain

$$\begin{aligned}
\boldsymbol{G} &= [-3L\cos\theta_1,\ \ -L\sin\theta_1,\ \ 1,\\
&\quad\ -L\cos\theta_1,\ \ -L\sin\theta_1,\ \ -1]^T,\\
\dot{\boldsymbol{G}} &= [3L\dot{\theta}_1\sin\theta_1,\ \ -L\dot{\theta}_1\cos\theta_1,\ \ 0,\\
&\quad\ L\dot{\theta}_1\sin\theta_1,\ \ -L\dot{\theta}_1\cos\theta_1,\ \ 0]^T.
\end{aligned}$$

Also, the force vector is expressed as

$$\begin{aligned}
\boldsymbol{f} &= [F^{\mathrm{ex}}, 0,\ -2k_\theta(\theta_1 - \theta_{1,0}) - F^{\mathrm{ex}}L\cos\theta_1,\\
&\quad\ 0, 0,\ -2k_\theta(\theta_{1,0} - \theta_1)]^T.
\end{aligned}$$

Plugging these expressions into Eq. (5), we finally obtain the equation of motion of the single unit cell as

$$\begin{aligned}
&(mL^2/2 + J/2 + 2mL^2\cos^2\theta_1)\ddot{\theta}_1\\
&\quad -mL^2\dot{\theta}_1^2\sin 2\theta_1 + k_\theta(\theta_1 - \theta_{1,0}) = -F^{\mathrm{ex}}L\cos\theta_1.
\end{aligned} \tag{6}$$

If we consider the quasistatic case (i.e., acceleration and velocity terms are much smaller compared to the external excitation and spring force terms), the force-displacement relationship can be derived as follows:

$$F^{\mathrm{ex}} = -\frac{k_\theta(\theta_1 - \theta_{1,0})}{L\cos\theta_1}. \tag{7}$$

Note that F^{ex} is the external force applied to the roller joint as shown in Fig. 2(b). Using Eq. (7) and the axial displacement expression $u = 4L(\sin\theta_{1,0} - \sin\theta_1)$, we can calculate the force-displacement response as shown in Fig. 2(c). We observe that the system exhibits strain softening behavior in the compressive region, whereas the system shows strain hardening response in the tensile domain. Also, it is interesting to find that this strain softening and hardening behavior can be tuned by controlling the initial folding angle, $\theta_{1,0}$.

B. Lumped-mass model

In this section, we introduce a lumped-mass model, in which a chain of origami cells is modeled as lumped masses connected by nonlinear springs [see Fig. 3(b)]. The strain softening behavior of the TMP unit cell considered herein leads to the following power-law relationship:

$$F^{\mathrm{ex}} = A\delta^n, \tag{8}$$

where δ is the compressive displacement, and the coefficient A and the exponent n are the constant values determined by curve fitting of Eq. (7).

Since the power-law relationship in Eq. (8) assumes only a positive displacement as an argument, we need to apply a displacement offset (denoted by d_0) toward the tension side, so that the lumped-mass model can approximate the force-displacement curve of the multibar linkage model not only in the compressive region, but also in the tensile domain. In Fig. 2(c), the dashed curve shows the fitted power-law relationship for the multibar linkage model, where the black circle represents (along the horizontal axis) the displacement offset d_0.

By using this simple force-displacement relationship, we can derive a general expression of the equation of motion as follows:

$$M\ddot{u}_j = A[d_0 + \delta_{j-1,j}]_+^n - A[d_0 + \delta_{j,j+1}]_+^n, \tag{9}$$

where M is the lumped mass corresponding to $2m$, $n \in \mathbb{R}$, and the bracket is defined by $[\cdot]_+ = \max(0,\cdot)$. Note that this form of equation has been used widely for analyzing nonlinear waves propagating in discrete systems in the case of strain-hardening interactions (i.e., $n > 1$ in Eq. (9), e.g., granular crystals). Therein, the formation and propagation of nonlinear wave structures, such as solitary waves [19,20] and discrete breathers [21,22], have been well studied. The interpretation of origami dynamics via this nonlinear lumped-mass system opens up a broad, novel potential vein of studies. Indeed, one advantage of modeling the origami lattice in this way is that many tools and results obtained in the context of granular crystals and, more generally, Fermi-Pasta-Ulam-type settings [25] can be applied in our system. For example, the recent work of Ref. [18] examined a one-dimensional discrete system under the power-law relationship of strain-softening springs (i.e., $n < 1$ in Eq. (9)). This study reported the propagation of rarefaction waves through dynamic simulations and a long wavelength approximation, where it was shown that the width of the rarefaction wave is independent of the wave speed. In the work of Ref. [23], a lattice of tensegrity structures was shown to be described by Eq. (9) with $n < 1$. In this setting rarefaction waves were also studied. The analysis of nonlinear waves in post-buckled structures has been also attempted using a similar discrete system [26].

In this article, we extend the theoretical results in such nonlinear-spring systems by introducing a systematic tool for the computation of numerically exact traveling waves, which will be discussed in Sec. IV. We also address the subject of their dynamical stability in Sec. V.

III. NUMERICAL SIMULATIONS

To examine the dynamic characteristics of the origami-based structure and compare the results from the two reduced models, we conduct numerical computations of wave propagation under a compressive impact. Also, we apply various amplitudes of impact force to the multibar linkage model in order to examine the speed of both compressive and tensile strain waves, especially focusing on the dominant traveling wave.

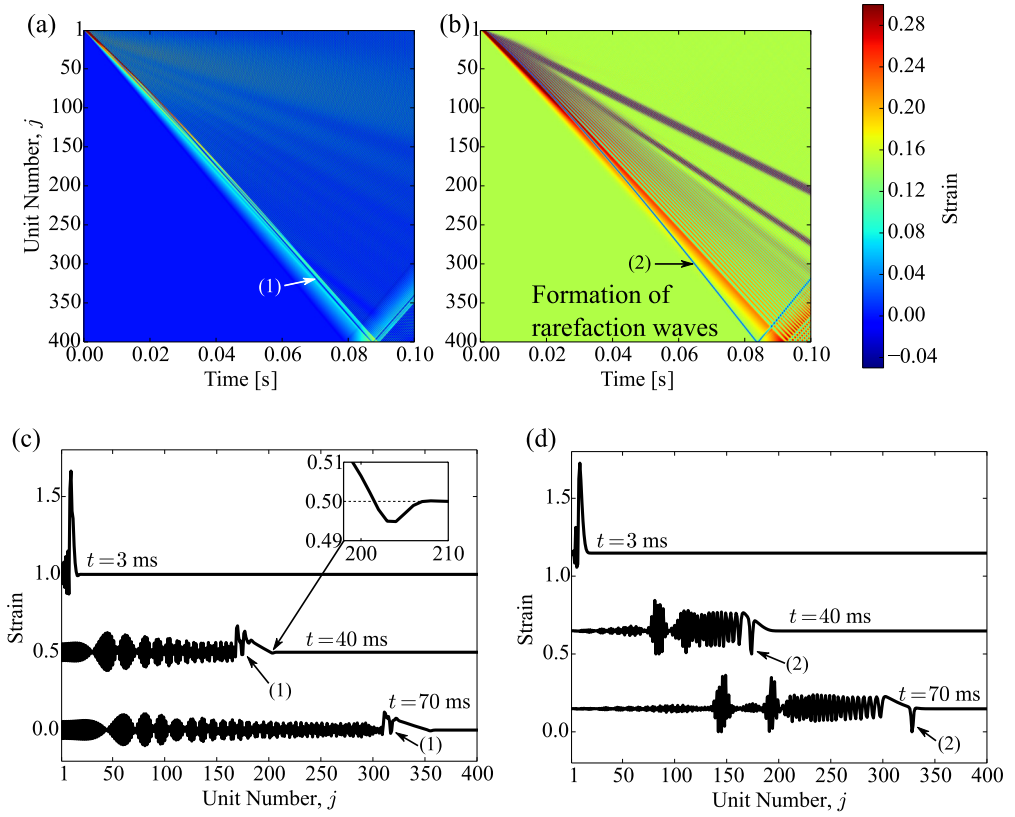

FIG. 4. Space-time contour plots of strain-wave propagation based on (a) the multibar linkage model and (b) the lumped-mass model. Temporal plots of strain waves using (c) the multibar linkage model and (d) the lumped-mass model. Strain curves at $t = 3$ ms and 40 ms are offset by 1.0 and 0.5, respectively, to ease visualization. The inset in (c) shows the magnified view of the leading edge. The arrows (1) and (2) point to the rarefaction wave present in the dynamics.

A. Waveform analysis

We perform numerical computations where a compressive impact is applied to the first unit cell with the right end of the Nth unit cell kept fixed as shown in Fig. 3(a). The strain waves propagating in a uniform chain of $N = 400$ unit cells are examined numerically. In the case of the multibar linkage model, the relative strain is defined as

$$\eta_j = \frac{h_{j,0} - h_j}{h_{j,0}}, \tag{10}$$

where $h_j = 4L \sin\theta_j$ and $h_{j,0} = 4L \sin\theta_{j,0}$ [see Fig. 2(b)]. The numerical constants used in the calculation are the following: $L = 5$ mm, $m = 0.39$ g, $k_\theta = 1.0$ Nm/rad, and $\theta_{j,0} = 45^\circ$. To apply impact excitation, we impose $F^{\text{ex}} = 100$ N for the first 1 ms and $F^{\text{ex}} = 0$ N after the first 1 ms in our simulations. From the force-displacement curve based on these constants, we obtain $n = 0.64$ and $A = 2{,}938$ N/m^n, given an initial displacement offset of $d_0 = 2.1$ mm for the power-law approximation. In the case of the lumped-mass model, the relative strain is defined as

$$\eta_j = \frac{u_{j+1} - u_j}{d_0}. \tag{11}$$

Figures 4(a) and 4(b) show space-time contour plots of strain-wave propagation under compressive impact, while Figs. 4(c) and 4(d) show the strain waveforms corresponding to $t = 3$,40, and 70 ms. Note that in Figs. 4(c) and 4(d), the strain curves at $t = 3$ and 40 ms are shifted vertically by 0.5 and 1, respectively, to ease visualization. After the impact force is applied to the system, the first compressive impact attenuates quickly as the strain waves propagate through the system, and then a rarefaction wave appears in front of the first compressive wave (see the arrows (1) and (2) in Fig. 4). It should be also noted that due to the strain-softening behavior, the amplitude of the compressive force is reduced drastically as the wave propagates along the chain. Since both the multibar linkage model and the lumped-mass model have this strain-softening nature, the analogous type of rarefaction waves is observed.

In addition, the inset of Fig. 4(c) shows the magnified view of the leading edge of the propagating strain wave. This leading wave is created due to the effect of inertia in the multibar linkage model. That is, when the first unit cell folds right after the compressive impact, the second unit cell is pulled by the first unit cell before the compressive force propagates to the next unit cell. Therefore, the tensile strain appears in front of the first compressive wave in the multibar linkage model. Comparing the numerical results of the two models, the lumped-mass model captures the multibar linkage model dynamics even quantitatively at short times, while the agreement between the two becomes qualitative at longer time scales (see, also, Appendix A, corresponding to the tensile impact case).

Let us also note in passing that in the wake of this primary rarefaction pulse, we observe radiative dispersive wave packets both in the multibar linkage model and in the lumped-mass

model. These wave packets apparently travel maximally with the speed of sound in the medium, while the rarefaction pulse outrunning them is apparently supersonic. We will return to this point to corroborate it further by our numerical bifurcation analysis in the next section. Additionally, it should be noted that in the lumped-mass model, highly localized structures with a clear envelope can be discerned (see, e.g., the vicinity of unit number 150 of the 70 ms panel of Fig. 4(d)), which seem to have the form of excitations, which are exponentially localized in space and periodic in time [27,28]. A closer inspection of Fig. 4(b) also seems to suggest that such coherent wave packets travel more slowly than the dispersive radiation. The multibar linkage model also exhibits such time-periodic patterns, but there is no clear signature of spatial localization. The fundamental difference of wave propagation between these two models stems from the fact that the lumped-mass model neglects rotational motions of origami components, while the multibar linkage model accounts for coupled motions of both translational and rotational dynamics of origami. While these nonlinear wave structures are worth investigating, this topic is beyond the scope of this paper, and we do not explore them further here.

B. Wave-speed analysis

The propagation speed of strain waves is now investigated numerically under various amplitudes of impact force. The wave speed is approximated as follows:

$$V_\varepsilon = \frac{N h_0}{\Delta t}, \tag{12}$$

where h_0 is the initial height of the unit cell, and Δt is the time span in which the strain wave propagates from the first unit cell to the Nth unit cell [see Fig. 5(a)]. The propagating wave speeds calculated are depicted in Fig. 5(b) under three different initial folding angles: $\theta_{j,0} = 35^\circ, 45^\circ$, and 55°. It is evident that the wave speed is altered by the impact force, which is one of characteristics of nonlinear waves. However, it should be noted that in the compressive regime, the wave speed decreases as the compressive impact increases. This is in sharp contrast to conventional nonlinear waves formed in the system of strain-hardening lattices [19,20]. A different trend is observed in the tensile regime, where the wave speed increases as the tensile impact increases. It is also noteworthy that the wave speed curve can be shifted by changing the initial folding angle. Therefore, we can control the speed of the waves propagating through the origami-based metamaterials by altering their geometrical configurations, implying their inherent dynamical tunability.

IV. EXACT RAREFACTION WAVES OF THE LUMPED MASS MODEL

We now turn our attention to a more systematic analysis and understanding of the rarefaction waves in the simpler lumped-mass model; notably, our conclusions here in that regard are of broader interest to previously discussed settings such as those of Refs. [18,23]. Based on the previous analysis, we numerically investigate the existence and dynamical stability of exact rarefaction waves of the lumped-mass model [cf. Eq. (9)]. In particular, we consider the model in the strain variable $\delta_{j,j+1}$ written as

$$M\ddot{\delta}_{j,j+1} = A\{[d_0 + \delta_{j-1,j}]_+^n - 2[d_0 + \delta_{j,j+1}]_+^n + [d_0 + \delta_{j+1,j+2}]_+^n\}. \tag{13}$$

The existence and the spectral stability of traveling waves of Eq. (13) with wave speed c must be examined through the ansatz $\delta_{j,j+1}(t) = \delta(j - ct) := \Phi(\xi,t)$, i.e., going to the cotraveling wave frame where the relevant solution appears to be steady and hence amenable to a spectral stability analysis. Then, Φ solves the advance-delay differential equation:

$$\Phi_{tt}(\xi,t) = -c^2\Phi_{\xi\xi}(\xi,t) + 2c\Phi_{\xi t}(\xi,t) + \frac{A}{M}\{[d_0 + \Phi(\xi-1,t)]_+^n - 2[d_0 + \Phi(\xi,t)]_+^n + [d_0 + \Phi(\xi+1,t)]_+^n\}. \tag{14}$$

Traveling waves of Eq. (13) correspond to stationary (time-independent) solutions $\Phi(\xi,t) = \phi(\xi)$ of Eq. (14), satisfying

$$0 = -c^2\phi_{\xi\xi} + \frac{A}{M}\{[d_0 + \phi(\xi-1)]_+^n - 2[d_0 + \phi(\xi)]_+^n + [d_0 + \phi(\xi+1)]_+^n\}. \tag{15}$$

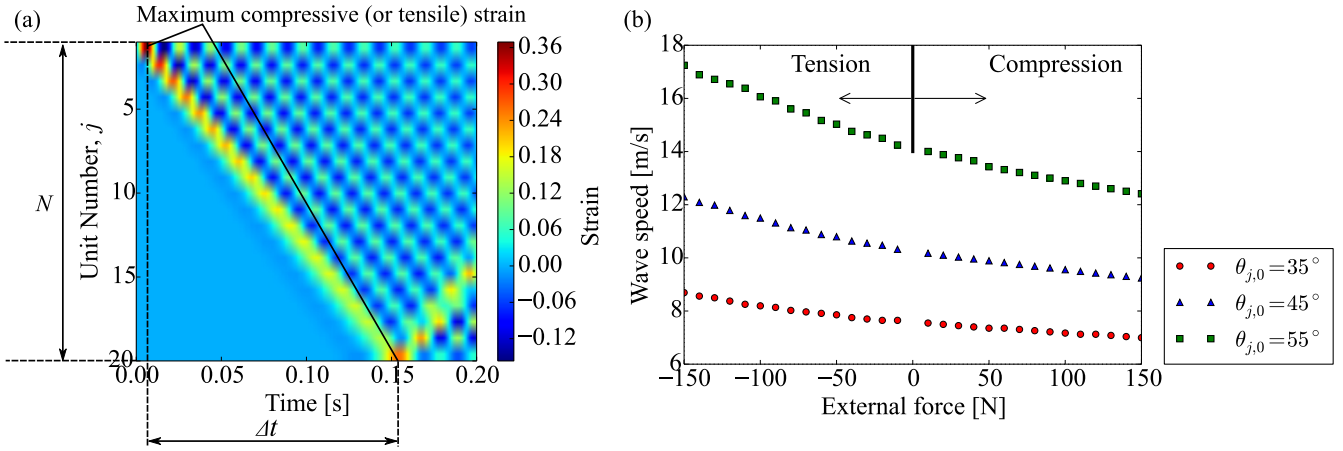

FIG. 5. (a) Surface map of strain field to calculate wave speed. (b) Wave speed of strain waves as a function of external force ranging from −150 N to +150 N. Numerical simulations are based on $L = 25$ mm, $m_j = 19.7$ g, $N = 20$, and $k_\theta = 1.0$ Nm/rad.

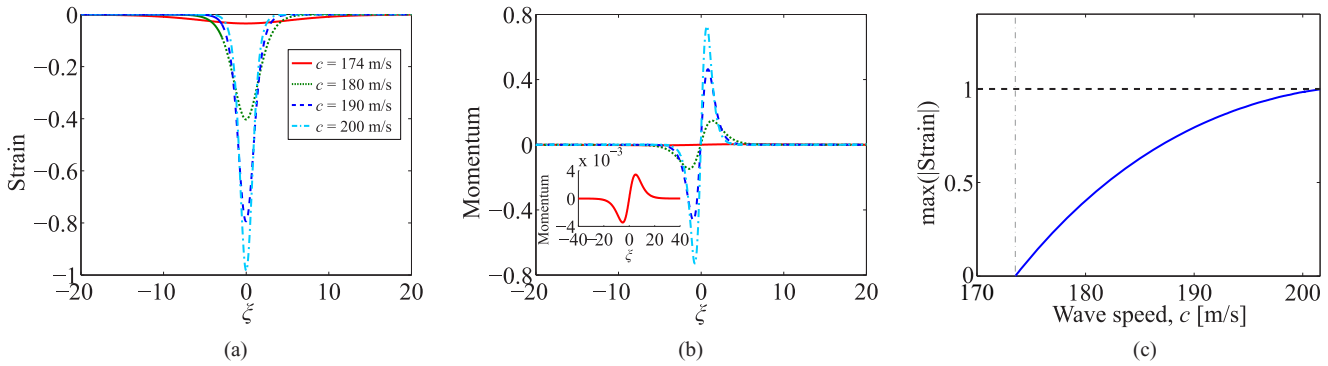

FIG. 6. Summary of numerical results on continuations of rarefaction waves over wave speed c with $l = 4001$ points and $\Delta\xi = 1/13$: (a) Relative strain profiles for various values of the wave speed c. (b) Relative momenta corresponding to (a). (c) Maximum of the absolute value of the relative strain variable as a function of the wave speed. Note that the horizontal dashed black line corresponds to the value of pre-compression in normalized units (or, equivalently, d_0 in physical units), while the vertical dashed-dot gray line corresponds to the value of the speed of sound c_s of the medium.

To obtain numerical solutions of Eq. (15), we employ a uniform spatial discretization of ξ consisting of l points ξ_k ($k = -\frac{l-1}{2}, \ldots, 0, \ldots, \frac{l-1}{2}$) with lattice spacing $\Delta\xi$ chosen such that $q = 1/\Delta\xi$ is an integer. Then, the field $\phi(\xi)$ is replaced by its discrete counterpart, i.e., $\phi_k := \phi(\xi_k) = \phi(k\Delta\xi)$. The second-order spatial derivative appearing in Eq. (15) is replaced by a modified central difference approximation $(\phi_{k-2} - 2\phi_k + \phi_{k+2})/(4\Delta\xi^2)$. The reason for this choice of central difference is connected to the stability calculation to be discussed in Sec. V. Using this discretization, Eq. (15) becomes the following root-finding problem,

$$0 = -c^2\frac{\phi_{k-2} - 2\phi_k + \phi_{k+2}}{4\Delta\xi^2} + \frac{A}{M}\{[d_0 + \phi_{k-q}]_+^n - 2[d_0 + \phi_k]_+^n + [d_0 + \phi_{k+q}]_+^n\}, \quad (16)$$

which is solved via Newton iterations. We employ periodic boundary conditions at the edges of the spatial grid. We are interested specifically in rarefaction waves, and thus we use the profiles obtained via the numerical simulations of Sec. III A to initialize the Newton solver; see, e.g., arrow (2) of Fig. 4(d). Herein, we consider an origami lattice with $L = 25$ mm, $k_\theta = 1.0$ Nm/rad and $\theta = 55^\circ$. The corresponding best-fit values of the parameters of the lumped-mass model are $A = 280\,\mathrm{N/m}^n$, $n = 0.53$, $m = 19.7$ g, with $M = 2m$ and $d_0 = 12$ mm.

In Fig. 6, numerically exact rarefaction waves (i.e., solutions of Eq. (16) with a prescribed tolerance) are presented for various values of the wave speed c. In particular, Fig. 6(a) shows the rarefaction waves in terms of the relative strain variable ϕ/d_0, while Fig. 6(b) shows the corresponding relative momenta ϕ'/d_0. Note that the tails decay to zero monotonically, implying that the traveling structure does not resonate with the linear modes of the system, as the wave is supersonic. It is not surprising then that our parametric continuation in the wave speed c reveals a critical minimum value $c_s = \sqrt{nAd_0^{n-1}/M} = 173.5$ m/s, which is the sound speed of the chain (see the vertical dashed-dot gray line of Fig. 6(c)). This is consistent with the long-wavelength analysis of Ref. [18] and also with our observations of the previous section, indicating that the wave outruns the small amplitude radiation tails behind it. Thus, similar to systems with $n > 1$ [19,29], the rarefaction waves of the origami lattice are traveling faster than any linear waves of the system. However, in contrast to solitary waves in systems with $n > 1$, the amplitude of the rarefaction waves in the origami system has a natural bound determined by the precompression d_0 of the system, in which case the particles come out of contact [see the horizontal dashed black line of Fig. 6(c)]. Although waves with amplitude exceeding this value are in principle possible, we were unable to identify any numerically. An interesting open problem would be to prove rigorously if such a bound exists. Another interesting related problem is if there is a critical maximum value of c. Our numerical continuation algorithm did indeed terminate due to lack of convergence at $c \approx 201.6$ m/s, but this could have been a result of the ill-conditioned nature of the Jacobian matrix as the amplitude approached the critical limit of d_0. Given the tunability of origami lattices (and associated nonlinear contact force exponents n), it would also be of interest to explore the variation of the above features over different values of n.

V. SPECTRAL AND DYNAMICAL STABILITY OF RAREFACTION WAVES

The robustness of a solution ϕ^0 of Eq. (15) can be investigated through a spectral stability analysis. Here we investigate the spectral and dynamical stability of rarefaction waves based on the analytical derivation in Sec. IV. To investigate the spectral stability of a solution ϕ^0 of Eq. (15), we substitute the linearization ansatz $\Phi(\xi,t) = \phi^0 + \varepsilon a(\xi)e^{\lambda t}$ into Eq. (14), yielding the eigenvalue problem at order ε:

$$\lambda^2 a(\xi) = -c^2 a_{\xi\xi}(\xi) + 2\lambda c a_\xi(\xi) + n\frac{A}{M}\{[d_0 + \phi^0(\xi-1)]_+^{n-1}a(\xi-1) - 2[d_0 + \phi^0(\xi)]_+^{n-1}a(\xi) + [d_0 + \phi^0(\xi+1)]_+^{n-1} \times a(\xi+1)\}, \quad (17)$$

where (λ, a) correspond to the eigenvalue-eigenvector pair. We define a solution ϕ^0 of Eq. (14) to be stable if none of the eigenvalues $\lambda = \lambda_r + i\lambda_i$ has a positive real part. The eigenvalue problem corresponding to the rarefaction wave

(in which ϕ^0 is localized in ξ) can be seen as a compact perturbation of the eigenvalue problem in which $\phi^0 = 0$. Thus, we expect the continuous spectra of these eigenvalue problems to coincide [30].

If $\phi^0 = 0$, then we can solve Eq. (17) analytically with the ansatz $a(\xi) = e^{i\xi\ell}$, where the eigenvalues are given by

$$\lambda(\ell) = i\ell c \pm 2i \sin\left(\frac{\ell}{2}\right)\sqrt{\frac{nAd_0^{n-1}}{M}}. \tag{18}$$

This indicates that the continuous spectrum around the uniform steady state is purely on the imaginary axis. Thus, any instability of the rarefaction wave will be due to point spectrum, which we must calculate numerically. We chose a discretization such that the spectra of the zero solution [see Eq. (18)] corresponds to the spectra of the zero solution of the discrete variant of Eq. (17). Using the standard central differences for the spatial derivatives appearing in Eq. (17) will lead to eigenvalues with a real part in the case of $\phi^0 = 0$. Hence, particular care needs to be taken to discretize the first and second derivative operators in a "compatible" way. Indeed, in order to avoid this "spurious instability," we used a modified central difference formula for the second spatial derivative, leading to the following eigenvalue problem:

$$\begin{aligned}
\lambda a_k &= b_k,\\
\lambda b_k &= -c^2\frac{a_{k+2} - 2a_k + a_{k-2}}{4\Delta\xi^2} + c\frac{b_{k+1} - b_{k-1}}{\Delta\xi}\\
&\quad + n\frac{A}{M}\left\{\left[d_0 + \phi^0_{k-q}\right]_+^{n-1} a_{k-q} - 2\left[d_0 + \phi^0_k\right]_+^{n-1} a_k\right.\\
&\quad \left. + \left[d_0 + \phi^0_{k+q}\right]_+^{n-1} a_{k+q}\right\},
\end{aligned} \tag{19}$$

which has been cast as a linear system in λ through the definition $a\lambda = b$ (such that standard eigenvalue solvers can be used), and where $a_k := a(k\Delta\xi)$. In the case of $\phi^0 = 0$, Eq. (19) with $k \in \mathbb{Z}$ is solved by $a_k = e^{ik\Delta\xi\ell}$, where the eigenvalues are given by

$$\lambda(\ell) = i\frac{\sin(\ell\Delta\xi)}{\Delta\xi}c \pm 2i \sin\left(\frac{\ell}{2}\right)\sqrt{\frac{nAd_0^{n-1}}{M}}, \tag{20}$$

which is consistent with Eq. (18) in the limit $\Delta\xi \to 0$ and perhaps even more importantly is also purely on the imaginary axis, suggesting neutral stability. However, additional inconsistencies may arise due to the finite nature of the computations and introduction of boundary conditions. For example, we find eigenvalues with a spurious real part in the base case of $\phi^0 = 0$ when fixed boundary conditions are used, whereas periodic boundary conditions retrieve the "correct" result, with the eigenvalues being purely imaginary. All of the above heavily predisposes us about the ill-conditioned nature of this eigenvalue problem and the extreme sensitivity of the relevant eigenvalues to perturbations, a feature that will become even more transparent in our following discussion regarding the traveling wave stability on top of the trivial state of $\phi^0 = 0$.

With the appropriate discretization and boundary conditions at hand, we now turn to the stability spectra for the nontrivial solutions $\phi^0 \neq 0$ of Eq. (16). Figure 7 shows the eigenvalue spectrum of a rarefaction wave with $c = 180$. In this case, there is an eigenvalue with real part $\lambda_r \approx 0.073$, implying

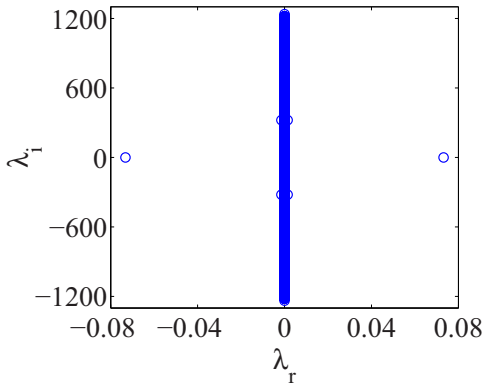

FIG. 7. Eigenvalue spectrum for a traveling wave with $c = 180$ and $d_0 = 12$ mm on a lattice with $l = 1501$ and $\Delta\xi = 0.2$.

the presence of either a spurious or genuine (albeit very weak) instability. Given the scale of the parameters for the origami lattice considered, the value of $\lambda_r \approx 0.073$ may be misleading, since for example, when normalizing the system parameters (see Appendix B), the same solution has $\lambda_r \approx 3.12 \times 10^{-5}$. However, the conclusion remains the same: either the solution is very weakly unstable, or there is a spurious instability. The latter would not be surprising, given the very delicate nature of the stability computations, as highlighted above even in the trivial case of the zero solution. It is worthwhile to note here that all solutions that we computed yielded a spectrum with at least one eigenvalue with a (relatively small) real part. In order to resolve this pending issue (of whether this is a true or a spurious instability), we have resorted to direct numerical simulations (i.e., an examination of the dynamical stability of the state) of the time evolution of the traveling wave in what follows.

In our numerical computations of Eq. (13), we have initialized the evolution by a numerically exact traveling wave solution perturbed by a small and uniformly distributed random noise (in the vicinity of the coherent structure) with $\varepsilon = 10^{-3} \times \max(|\delta_{j,j+1}(t = 0)|)$. Remarkably, *all* the solutions we dynamically simulated appeared robust against such perturbations, suggesting the spectrally observed weak instabilities are spurious in this case. Figure 8 summarizes our findings on dynamical evolutions of rarefaction waves in terms of the relative strain variable $\delta_{j,j+1}(t)/d_0$, by illustrating the representative cases with wave speeds $c = 174$, 180, and 190. While outside the scope of the present article, an important future direction would be to develop more sophisticated discretization schemes (such as those based on Chebyshev collocation methods [31]) or algorithms for nonlinear eigenvalue problems (such as Jacobi-Davidson-type methods [32,33]) not only for the stability of rarefaction waves in the origami lattice, but also for a wide class of lattice dynamical systems supporting traveling waves.

VI. CONCLUSIONS AND FUTURE CHALLENGES

In the present work, we investigated nonlinear wave dynamics in origami-based metamaterials consisting of building blocks based on TMP cells. We analyzed the kinematics of the TMP unit cell using a simple multibar linkage model and

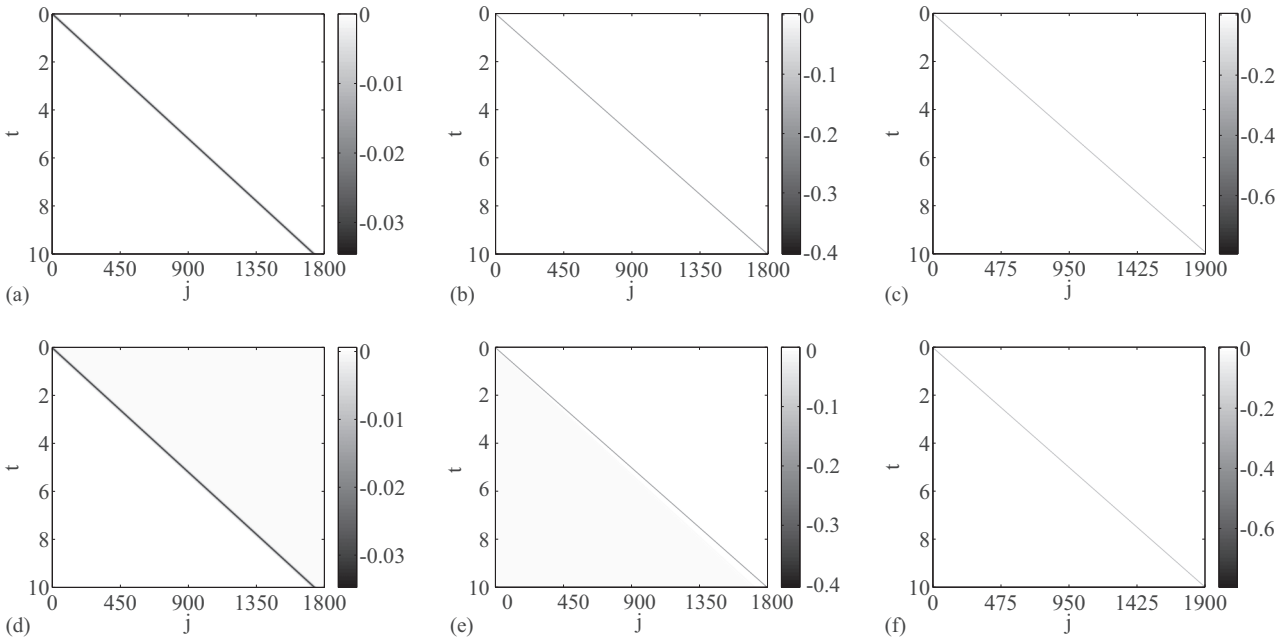

FIG. 8. Evolution of unperturbed (a)–(c) and perturbed (d)–(f) rarefaction waves with wave speed (a) and (d) $c = 174$, (b) and (e) $c = 180$, and (c) and (f) $c = 190$, respectively, according to the discrete equation [Eq. (13)] with periodic boundary conditions. The parameter values used are the same as those described in the caption of Fig. 7.

found that it exhibits tunable strain-softening behavior under compression due to its geometric nonlinearity. We observed that upon impact, this origami-based structure supports the formation and propagation of rarefaction waves. The resulting evolution features a tensile wavefront despite the application of compressive impact. A further reduction was also offered based on the fitted force-displacement formula for a single cell, in the form of a lumped-mass model. In the latter case we obtained numerically exact rarefaction waves and studied their spectral and especially dynamical stability. The dynamical features observed herein may constitute a highly useful feature toward the efficient mitigation of impact by converting compressive waves into rarefaction waves and disintegrating high-amplitude impulses into small-amplitude oscillatory wave patterns. We also demonstrated the potential tunability of the wave speed by altering initial folding conditions of the origami-based structure, which naturally opens up the feasibility of controlling stress wave propagation in an efficient manner.

The rather unique nonlinear wave dynamics of origami structures can lead to a wide range of applications, such as tunable wave transmission channels and deployable impact mitigating layers for space and other engineering systems. These applications will leverage the intrinsic versatility of origami structures, e.g., the formation of not only rarefaction waves, but also other types of nonlinear waves and tunable frequency band structures. On the theoretical and computational side, there is also a large number of intriguing questions that are emerging. For example, a more detailed comparison of the coherent wave structures propagating in the multibar linkage model versus the lumped-mass model would be an interesting topic for further consideration. This would help uncover the dynamical features leading to the apparent weak amplitude decay in the former, in contrast to the robust wave propagation in the latter. At the single-wave level, an exploration of the delicate issues of spectral stability by means of different numerical methods and of the corresponding dynamical implications would be of particular interest. Subsequently, understanding the dynamics and interactions of multiple rarefaction wave patterns would also be a relevant theme for future investigations. These topics are currently under active consideration and will be reported in future publications.

ACKNOWLEDGMENTS

J.Y. acknowledges the support of NSF (Grant No. 1553202), ONR (Grant No. N000141410388), and ADD of Korea (Grant No. UD140059JD). J.Y. and P.G.K. acknowledge the support of ARO (Grant No. W911NF-15-1-0604). E.G.C. and P.G.K. acknowledge support from the US-AFOSR under Grant No. FA9550-12-10332. P.G.K. also acknowledges support from the NSF under Grant No. DMS-1312856, from ERC and FP7-People under Grant No. 605096, and from the Binational (US-Israel) Science Foundation through Grant No. 2010239. P.G.K.'s work at Los Alamos is supported in part by the U.S. Department of Energy. The work of C.C. was partially supported by the ETH Zurich Foundation through the Seed Project No. ESC-A 06-14.

APPENDIX A: COMPARISON BETWEEN MULTIBAR LINKAGE AND LUMPED-MASS MODELS UNDER TENSILE IMPACT

In Fig. 4, we show the comparison between multibar linkage and lumped-mass models under compressive impact. Here, we turn our attention to the case of *tensile* impact. For numerical simulations, we applied an impact of $F^{\text{ex}} = -100$ N (minus sign indicates tensile direction) during the time span of 1 ms.

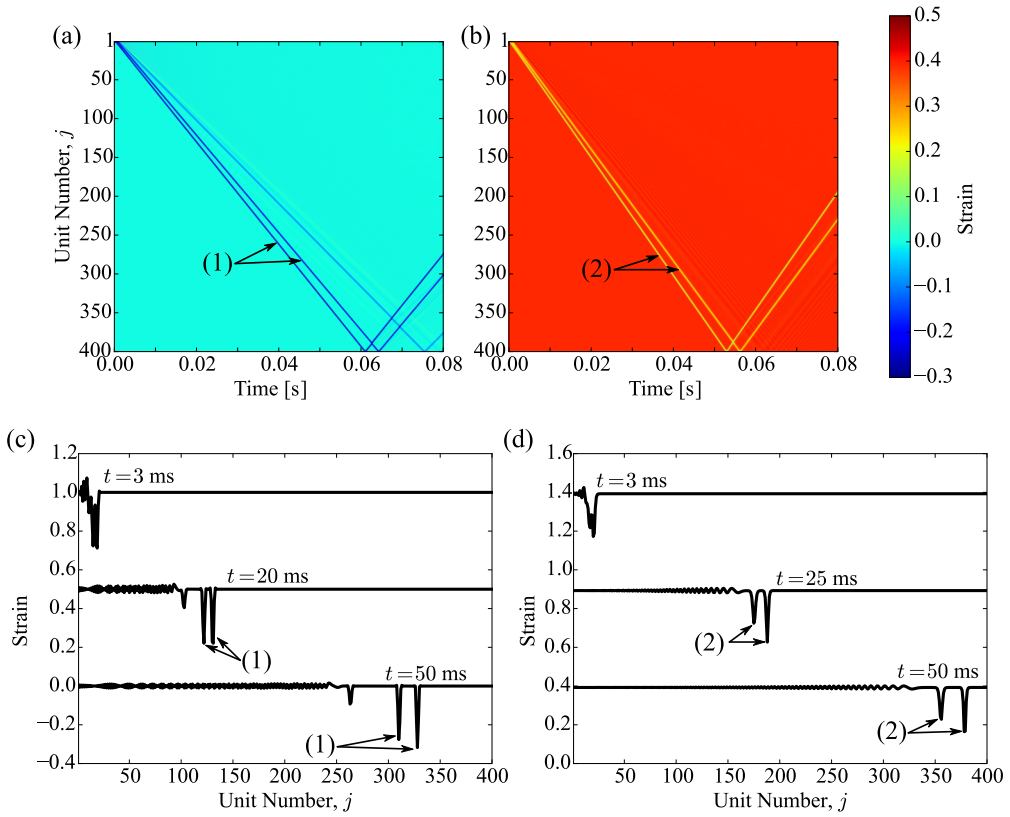

FIG. 9. Space-time contour plots of strain-wave propagation under tensile impact based on (a) the multibar linkage model and (b) the lumped-mass model. Temporal plots of strain waves using (c) the multibar linkage model and (d) the lumped-mass model. Strain curves at $t = 3$ ms and 20 ms are offset by 1.0 and 0.5, respectively, to ease visualization. The inset in (c) shows the magnified view of the leading edge. The arrows (1) and (2) point to the solitary wave packets present in the dynamics.

The numerical constants used in the multibar linkage model are the same as described in Sec. III. For the lumped-mass model, we obtain $n = 0.22$ and $A = 2{,}815\,\mathrm{N/m}^n$, given an initial displacement offset of $d_0 = 5.6\,\mathrm{mm}$ for the power-law approximation. Figures 9(a) and 9(b) show space-time contour plots of strain-wave propagation under compressive impact, while Figs. 9(c) and 9(d) show the strain waveforms corresponding to $t = 3, 20$, and 50 ms. Both the multibar linkage model and lumped-mass model exhibit tensile isolated waves propagating faster than the other oscillatory waves. These waveforms look similar to those of solitary waves formed in granular crystals, except that they exhibit tensile packets instead of compressive ones [19]. The simulation results in Fig. 9 imply that both numerical approaches—the lumped-mass model and the multibar linkage model—produce qualitatively analogous results given the parameters used in our origami-based metamaterial system. This verifies the validity of the quasistatic approach used in the lumped-mass model through this qualitative agreement. We also note that quantitative aspects still retain a number of distinctive features between the two models. For example, the multibark linkage model has more such isolated waves (i.e., notice a smaller one around $j = 260$ in panel (c)), and the difference in speed between the isolated waves and the oscillatory tail is clearly larger in panel (c) in comparison to panel (d) of the lumped-mass model.

APPENDIX B: LUMPED-MASS MODEL IN SCALED UNITS

We shortly discuss the scaling transformation applied to the model equation [Eq. (19)]. The latter can be written as

$$\ddot{\tilde{\Phi}}_k = -c^2\frac{\tilde{\Phi}_{k+2} - 2\tilde{\Phi}_k + \tilde{\Phi}_{k-2}}{4\Delta\xi^2} + c\frac{\dot{\tilde{\Phi}}_{k+1} - \dot{\tilde{\Phi}}_{k-1}}{\Delta\xi} + \frac{A}{M}\{[d_0 + \tilde{\Phi}_{k-q}]_+^n - 2[d_0 + \tilde{\Phi}_k]_+^n + [d_0 + \tilde{\Phi}_{k+q}]_+^n\}. \tag{B1}$$

Then, both the strain and time variables are rescaled using $\tilde{\Phi} \mapsto \tilde{\Phi}/\alpha$ and $t \mapsto \beta t$, respectively, where the scaling factors are given by $\alpha = d_0$ and $\beta = \sqrt{\alpha^{n-1}A/M}$. This way, Eq. (B1) is written in scaled units as

$$\ddot{\tilde{\Phi}}_k = -\tilde{c}^2\frac{\tilde{\Phi}_{k+2} - 2\tilde{\Phi}_k + \tilde{\Phi}_{k-2}}{4\Delta\xi^2} + \tilde{c}\frac{\dot{\tilde{\Phi}}_{k+1} - \dot{\tilde{\Phi}}_{k-1}}{\Delta\xi} + \{[1 + \tilde{\Phi}_{k-q}]_+^n - 2[1 + \tilde{\Phi}_k]_+^n + [1 + \tilde{\Phi}_{k+q}]_+^n\}, \tag{B2}$$

with the scaled wave speed given by $\tilde{c} = c/\beta$.

[1] O. Mori, H. Sawada, R. Funase, M. Morimoto, T. Endo, T. Yamamoto, Y. Tsuda, Y. Kawakatsu, J. Kawaguchi, Y. Miyazaki, and Y. Shirasawa, IKAROS Demonstration Team, and Solar Sail Working Group, *Transactions of the Japan Society for Aeronautical and Space Sciences, Aerospace Technology Japan 8*, To_4_25 (Japan Society for Aeronautical and Space Science, Tokyo, Japan, 2010).

[2] Y. Tsuda, O. Mori, R. Funase, H. Sawada, T. Yamamoto, T. Saiki, T. Endo, and J. Kawaguchi, Flight Status of IKAROS Deep Space Solar Sail Demonstrator, Acta Astronaut. **69**, 833 (2011).

[3] S. A. Zirbel, R. J. Lang, M. W. Thomson, D. A. Sigel, P. E. Walkemeyer, B. P. Trease, S. P. Magleby, and L. L. Howell, Accommodating Thickness in Origami-Based Deployable Arrays, J. Mech. Des. **135**, 111005 (2013).

[4] H. Kobayashi, B. Kresling, and J. F. V. Vincent, The Geometry of Unfolding Tree Leaves, Proc. R. Soc. Lond. B **265**, 147 (1998).

[5] I. Mikó, R. S. Copeland, J. P. Balhoff, M. J. Yoder, and A. R. Deans, Folding wings like a cockroach: A review of transverse wing folding ensign wasps (Hymenoptera: Evaniidae: Afrevania and Trissevania), PLoS One **9**, e94056 (2014).

[6] K. Miura, in *Proceedings of the IASS Symposium on Folded Plates and Prismatic Structures*, edited by R. Krapfenbauer (Eigentümer, Vienna, Austria, 1970).

[7] See http://www.kirin.co.jp/products/rtd/hyoketsu/

[8] M. Schenk and S. D. Guest, Geometry of Miura-folded Metamaterials, Proc. Natl. Acad. Sci. U.S.A. **110**, 3276 (2013).

[9] Z. Y. Wei, Z. V. Guo, L. Dudte, H. Y. Liang, and L. Mahadevan, Geometric Mechanics of Periodic Pleated Origami, Phys. Rev. Lett. **110**, 215501 (2013).

[10] K. Cheung, T. Tachi, S. Calisch, and K. Miura, Origami Interleaved Tube Cellular Materials, Smart Mater. Struct. **23**, 094012 (2014).

[11] H. Yasuda and J. Yang, Reentrant Origami-Based Metamaterials with Negative Poisson's Ratio and Bistability, Phys. Rev. Lett. **114**, 185502 (2015).

[12] M. Schenk, S. D. Guest, and G. J. McShane, Novel Stacked Folded Cores for Blast-resistant Sandwich Beams, Int. J. Solids Struct. **51**, 4196 (2014).

[13] K. Miura and T. Tachi, in *Symmetry Art Sci. 2010/1-4, Spec. Issues Festival-Congress*, ISIS-Symmetry (International Soc. Interdiscip. Study Symmetry) Gmuend, Austria (2010), pp. 204–213.

[14] T. Tachi, in *Proceedings of the International Association for Shell and Spatial Structures (50th. 2009. Valencia). Evolution and Trends in Design, Analysis and Construction of Shell and Spatial Structures*, edited by A. Domingo and C. Lazaro (Editorial de la Universitat Politécnica de Valencia, Valencia, 2010), pp. 2295–2305.

[15] K. Miura, Method of packaging and deployment of large membranes in space, Inst. Space Astronaut Sci. Rep. **618**, 1 (1985).

[16] E. Falcon, C. Laroche, and S. Fauve, Observation of Depression Solitary Surface Waves on a Thin Fluid Layer, Phys. Rev. Lett. **89**, 204501 (2002).

[17] P. D. Lax, *Hyperbolic Systems of Conservation Laws and the Mathematical Theory of Shock Waves* (New York University, New York, 1973).

[18] E. B. Herbold and V. F. Nesterenko, Propagation of Rarefaction Pulses in Discrete Materials with Strain-softening Behavior, Phys. Rev. Lett. **110**, 144101 (2013).

[19] V. F. Nesterenko, *Dynamics Of Heterogeneous Materials* (Springer-Verlag, New York, 2001).

[20] S. Sen, J. Hong, J. Bang, E. Avalosa, and R. Doney, Phys. Rep. **462**, 21 (2008).

[21] G. Theocharis, N. Boechler, and C. Daraio, in *Phononic Crystals and Metamaterials* (Springer Verlag, New York, 2013), Chap. 6.

[22] P. G. Kevrekidis, IMA J. Appl. Math. **76**, 389 (2011).

[23] F. Fraternali, G. Carpentieri, A. Amendola, R. E. Skelton, and V. F. Nesterenko, Multiscale tunability of solitary wave dynamics in tensegrity metamaterials, Appl. Phys. Lett. **105**, 201903 (2014).

[24] F. C. Moon, *Applied Dynamics: With Applications to Multibody and Mechatronic Systems* (Wiley, New York, 1998).

[25] E. Fermi, J. Pasta, and S. Ulam, Tech. Rep. Los Alamos Nat. Lab. LA1940 (1955); D. K. Campbell, P. Rosenau, and G. M. Zaslavsky, Chaos **15**, 015101 (2005); G. Galavotti (Ed.) *The Fermi-Pasta-Ulam Problem: A Status Report* (Springer-Verlag, New York, 2008).

[26] F. Maurin and A. Spadoni, Low-frequency wave propagation in post-buckled structures, Wave Motion **51**, 323 (2014).

[27] S. Flach and A. V. Gorbach, Discrete breathers: Advances in theory and applications, Phys. Rep. **467**, 1 (2008).

[28] S. Aubry, Discrete Breathers: Localization and transfer of energy in discrete Hamiltonian nonlinear systems, Physica D **216**, 1 (2006).

[29] A. Stefanov and P. Kevrekidis, Nonlinearity **26**, 539 (2013).

[30] T. Kato, *Perturbation Theory for Linear Operators* (Springer-Verlag, Berlin, 1976).

[31] D. Gottlieb and S. A. Orszag, *Numerical Analysis of Spectral Methods: Theory and Applications*, SIAM, Philadelphia, 1977.

[32] F. Tisseur and K. Meerbergen, The quadratic eigenvalue problem. SIAM Rev. **43**, 235 (2001).

[33] G. L. G. Sleijpen, J. G. L. Booten, D. R. Fokkema, and H. A. van der Vorst, Jacobi-Davidson type methods for generalized eigenproblems and polynomial eigenproblems, BIT **36**, 595 (1996).